"A PROBABILITY ELECTRICAL RESISTIVITY TOMOGRAPHY IMAGING OF COMPLEX TECTONIC FEATURES IN THE KISSAMOS AND PALEOHORA URBAN AREAS, WESTERN CRETE (GREECE) "

Marilena Cozzolino[*,1,2], Paolo Mauriello[2], Margarita Moisidi[3], Filippos Vallianatos[3,4]

[1] Institute of Technologies Applied to Cultural Heritage, Cosiglio Nazionale delle Ricerche, Monterotondo St., Roma, Italia, www.itabc.cnr.it
[2] Department of Human, Social and Educational Science, University of Molise, Campobasso, Italy, www.unimol.it
[3] UNESCO Chair on Solid Earth Physics and Geohazards Risk Reduction, Hellenic Mediterranean University, Crete, Greece, http://www.hmu.gr
[4] Department of Geophysics–Geothermics, Faculty of Geology and Geoenvironment, National and Kapodistrian University of Athens, Greece, http://www.geol.uoa.gr

ABSTRACT

A number of 2D Electrical Resistivity Tomographies (ERT) was conducted in northwest and southwest Crete with the aim to model geo-tectonic features at selected urban sites. The study area is located within the central forearc of the Hellenic subduction zone. Thirteen ERT profiles were realized using the dipole-dipole electrode and/or the Wenner-Schlumberger arrays. In order to model the resistivity distribution, the probability-based electrical resistivity tomography inversion (PERTI) method has been applied. The main features of the PERTI method are: (i) unnecessity of a priori information; (ii) full, unconstrained adaptability to any kind of dataset, including the case of non-flat topography; (iii) independence from data acquisition techniques and spatial regularity; (iv) capability to resolve complex continuous resistivity variation. Since the present case-study is the first application of the PERTI algorithm to locate fault zones and near subsurface irregularities, its routine has been tested using the well-known RES2DINV commercial software as reference. The comparison has shown a common coherence between the results of the two inversion methods and confirmed the better filtering capacity and greater versatility of the PERTI algorithm, already outlined in a number of previous papers dealing with archaeological applications.

1. INTRODUCTION

Several geophysical techniques have been applied worldwide to experimentally determine fault zones and to provide a detailed image of the near subsurface structures in urban environment. In recent years, a large number of electrical resistivity tomographic surveys has been conducted to map fault zones [Storz et al., 2000; Demanet et al., 2001; Lapenna et al., 2003; Rizzo et al., 2004; Nguyen et al., 2007; Caputo et al., 2007; Margiotta and Negri, 2008; Martinez et al., 2009]. In the frame of this study, the probability electrical tomography imaging approach [Patella, 1997; Mauriello and Patella, 1999; Alaia et al., 2008; Mauriello and Patella, 2009] is tested using electrical resistivity data in Kastelli-Kissamos basin (northwest Crete) and Paleohora basin (southwest Crete). Data were acquired in order to model tectonic features and to reveal fault zones [Moisidi, 2009; Moisidi et al., 2013], within or nearby urban areas that are heavy populated mainly during summer season.

The use of geoelectrical inversion algorithms in highly articulated case studies from a geological point of view is certainly a very complex problem. Furthermore, it must be considered that the 2D inversion of geoelectrical profiles, in situations that may be very different from the assumed two-dimensionality, can lead to difficulties in interpretation, even relevant. In areas with very complex geology, there could be significant lateral (or horizontal) variations in the subsurface resistivity, which could cause distortions in the 2-D model obtained that might be, and frequently are, misinterpreted as changes with depth in the subsurface resistivity [Loke, 2004]. To model complex situations, extremely strong constraints must be introduced in the inversion routine. To this purpose, many methods have been proposed over the past two decades, following the classic deterministic approach to solve the problem [Sasaki, 1994; Loke and Barker, 1996; Tsourlos and Ogilvy, 1999; Dahlin, 2001; Papadopoulos et al., 2006, 2007, 2011; Pidlisecky et al., 2007; Marescot et al., 2008].

The fundamental aspect is that, in the classical procedures of inversion, a purely deterministic role is assigned to the interpretation process in contrast with the nature of uncertainty that is instead inherent in the process of geophysical measurement and on the basis of which there is the principle of equivalence. Thus, several models can generate the same set of data within the experimental error, albeit small, connected to the measurement. This means that the answer that such software give as output is not the solution of the particular problem as a whole, but of a subclass of it, that is of that problem bound by a starting model chosen a priori as input to the process: if the starting model changes, the final result changes. Moreover, in the case of very complex situations, the introduction of constraints contributes to increasing the non-univocal nature of the result.

An example is found in the previous work [Moisidi, 2009; Moisidi et al., 2013] where the interpretive results obtained with different acquisitions (the dipole-dipole electrode and the Wenner-Schlumberger arrays) on the same line lead to significantly different sections. As the PERTI algorithm can deal with multiple datasets, independently of the technique used for their acquisition, it also acts as an intrinsic filter. The result is the simultaneous smoothing of the uncorrelated noise and suppression of any correlated phantom effects. In principle, this property derives from the circumstance that such types of disturbances have zero probability of being associated with true anomaly sources within the context of the geoelectrical theory.

The purpose of this work is therefore to verify whether the application of a probability algorithm for resistivity tomography, even within the limits of a non-deterministic reconstruction of the subsoil section, can actually eliminate at least the ambiguity of interpretation of the different acquisition techniques, thus contributing to the definition of the geology of the area. Furthermore, the work aims to provide evidence that PERTI algorithm can minimize images created due to the presence of noise and/or correlated uncertain effects, as commonly appeared in complex near surface urban geo-structures.

The PERTI routine has been compared with the results obtained using the well-known RES2DINV commercial software [Loke, 2004] (www.geotomosoft.com), in which the inversion procedures are based on the smoothness-constrained least squares method [e.g Constable et al., 1987; Tsourlos, 1995; Loke and Barker, 1995; Loke and Barker, 1996a, 1996b] and the forward resistivity calculations were executed by applying an algorithm based on a Finite Element Method (FEM). ERT data were filtered and corrected for anomalous trends and simultaneously inverted for reconstructing the final tomographic model. RMS error is generally used to indicate the quality of the measurement. However, large contrasts in resistivity could insert high RMS errors (>40%) because of numerical instability of the final tomographic solution.

In the following sections, we report a short outline of PERTI method [Mauriello and Patella, 2009] as described in Cozzolino et al. [2014], we describe at first the geological background of Kissamos and Paleohora basins and the ERT acquisition plan, then the PERTI results, the results obtained using the renowned RES2Dinv inversion software (www.geotomosoft.com) and their comparison.

2. OUTLINE OF THE PERTI METHOD

The PERTI method is a straight derivation of the probability tomography imaging approach in which the spatial behavior of the resistivity anomaly occurrence probability function $\eta(P_q)$ is mapped and calculated at a grid of points P_q $(q = 1, 2, \ldots, Q)$ below the ground surface [Patella 1997; Mauriello and Patella, 1999; Alaia et. al., 2008]:

$$\eta(P_q) = C_q \sum_{m=1}^{M} \sum_{j_m=}^{J_m} \left[\rho_a(P_{j_m}) - \bar{\rho} \right] \Psi(P_{j_m}, P_q) \quad (1)$$

In equation (1), $\rho_a(P_{j_m})$ is the measured apparent re-

sistivity at P_{j_m}, that is, the j_mth nodal attribution point of the mth profile $(j_m = 1, \ldots, J_m; m = 1, \ldots, M)$; $\hat{\rho}$ is a pre-assigned resistivity of a homogeneous, isotropic half-space assumed as reference model; C_q is a positive-definite non-null normalization factor; $\Psi(P_{j_m}, P_q)$, often called the sensitivity function of the array, is the j_mth Frechet derivative referred to the reference model.

It physically describes the effect generated at P_{j_m} by a small perturbation of the reference resistivity at P_q, under Born approximation [Loke and Barker, 1995; Mauriello and Patella, 1999].

In practice, the average apparent resistivity is assumed as the reference uniform resistivity $\hat{\rho}$. Therefore, $\eta(P_q)$ is interpreted as an occurrence probability measure of a resistivity deviation from $\hat{\rho}$ at P_q. Positive or negative values of $\eta(P_q)$ give the occurrence probability of an increase or decrease of resistivity, respectively.

The starting assumption for the PERTI method is that the reference uniform resistivity $\hat{\rho}$ must not be pre-assigned as the mean value of all of the measured apparent resistivities, but assumed to be the unknown true resistivity value ρ_q belonging to q-th cell centred at P_q. With such an assumption, $\eta(P_q)$ given in equation (1) can be rewritten in compact form as

$$\eta(P_q) = C_q \sum_{m=1}^{M} \sum_{j_m=}^{J_m} \left[\rho_a(P_{j_m}) - \rho_q\right] \Psi(P_{j_m}, P_q) \qquad (2)$$

The rationale for the PERTI approach is that if $\eta(P_q) = 0$ resulted at P_q, then in the cell around P_q the most probable real resistivity would be exactly ρ_q. Thus, referring to equation (2), since it is always $C_q \neq 0$, the $\eta(P_q) = 0$ condition allows the following inversion formula to be easily derived (Mauriello and Patella 2009):

$$\rho_q = \frac{\displaystyle\sum_{m=1}^{M} \sum_{j_m=}^{J_m} \rho_a(P_{j_m}) \Psi(P_{j_m}, P_q)}{\displaystyle\sum_{m=1}^{M} \sum_{j_m=}^{J_m} \Psi(P_{j_m}, P_q)} \qquad (3)$$

The most probable real resistivity ρ_q at P_q, compatibly with data accuracy and density and within the assumed first order Born approximation, is nothing but a weighted average of the apparent resistivity values, using as weights the first-order Frechet derivatives, which depend on the coordinates of the chosen point [Barker, 1992]. A direct consequence of not requiring a priori information and iterative processes is, for the PERTI method, the uselessness of the computation of

the RMS error between measured and modelled apparent resistivity values. In fact, the resulting RMS error, whatever it is, can never be lowered within the PERTI scheme. Therefore, a way to judge the modelling capability of the PERTI method is the comparison of its results with those from any of the standardized deterministic inversion tools.

3. CASE STUDIES

Several geophysical techniques have been applied worldwide to experimentally determine fault zones and to provide a detailed image of the near subsurface structures in urban environment. In recent years, a large number of electrical resistivity tomographic surveys have been conducted to map fault zones [Storz et al., 2000; Demanet et al., 2001; Lapenna et al., 2003; Rizzo et al., 2004; Nguyen et al., 2007; Caputo et al., 2007; Margiotta and Negri, 2008; Martinez et al., 2009]. In the frame of this study, the probability electrical tomography imaging approach is testified using electrical resistivity data in Kastelli-Kissamos basin (northwest Crete) and Paleohora basin (southwest Crete), acquired in order to model tectonic features and to reveal fault zones [Moisidi, 2009; Moisidi et al., 2013], within or nearby urban areas that are heavy populated mainly during summer season.

The study area is located in western Crete (Figure 1) within the central outer forearc of the Hellenic subduction zone. The active tectonic of the area is characterized by the African plate motion relative to Eurasia [e.g Meier et al., 2007] and is characterized by N-S extension in the late Neogene E-W striking normal faults and ENE-WSW striking, left-lateral strike-slip faults, [e.g ten Veen and Postma 1999a, 1999b; Fassoulas et al., 2001; ten Veen and Kleinspehn, 2003], and late Tortorian to early Messinian E-W extension N-S oriented normal fault zones, [e.g van Hinsbergen and Meulenkamp, 2006]. In northwest and southwest Crete the extensional basins, filled with breccio-conglomerates, are complex multi-fractured neotectonic small scale half-graben basins bounded by N-S fault zones. Moreover, they are bounded by a W-E trending normal fault, and they can be characterized as alluvial fan, submarine steep-faced and basin-plain environments [Seidel et al., 2007]. The characteristic of the basins in these two localities is the subparallel fault blocks mountains separated by broad alluvium-filled half-graben [van Hinsbergen, 2006; Seidel et al., 2007]. The geology of Kastelli-Kissamou and Paleohora are derived from the Institute for Geology and

Subsurface Research and the Institute of Geology and Mineral Exploration, respectively.

ERT data were collected using an IRIS-Syscal Jr. Switch 48 instrument that features 48 electrodes, enabling fully automated measurements of the apparent subsurface resistivity, including dipole-dipole (DD) and Wenner-Schlumberger (WS) configurations. A detailed description is given in Moisidi [2009] and Moisidi et al. [2012, 2013]. In order to accommodate the wide resistivity range detected inside the data sets and to better show order of magnitude changes frequently appeared, a common logarithmic scale has been used for visualization of both apparent resistivity and modelled real resistivity maps [for the use of logarithmic scales in geoelectrics, see, e.g., Chambers et al., 2006].

3.1 KASTELLI-KISSAMOS AREA

The geology of the investigated sites in Kastelli-Kissamos area (Figure 2) is characterized by:

a) Recent beach deposits and sand dunes (Holocene) close to the coast (Quaternary);

b) Holocene alluvial deposits of loose loam, clay, sand and gravel of thickness not exceeding 3 m along the coast (Quaternary);

c) Pleistocene older fluvial terraces in the central and southern parts of the Basin (loose - unconsolidated deposits of red brownish clay containing a large percentage of sand, granules and pebbles and sometimes boulders sourced from limestones, hornfels and rarely from flysch sandstone); some beds of the older fluvial terraces are alternating shales and argillaceous sandstones;

d) Marly limestones (Middle Miocene);

e) Marls (while and yellowish and at the deeper part greenish alternating with marly sanstones and banks of marly limestone; Gypsum (G) (Middle Miocene);

f) Conglomerates (pebbles mainly of Mesozoic limestones (Middle Miocene);

g) Flysch (alternating beds of shales and arqillaceous sandstones - Upper Cretaceous to Eocene);
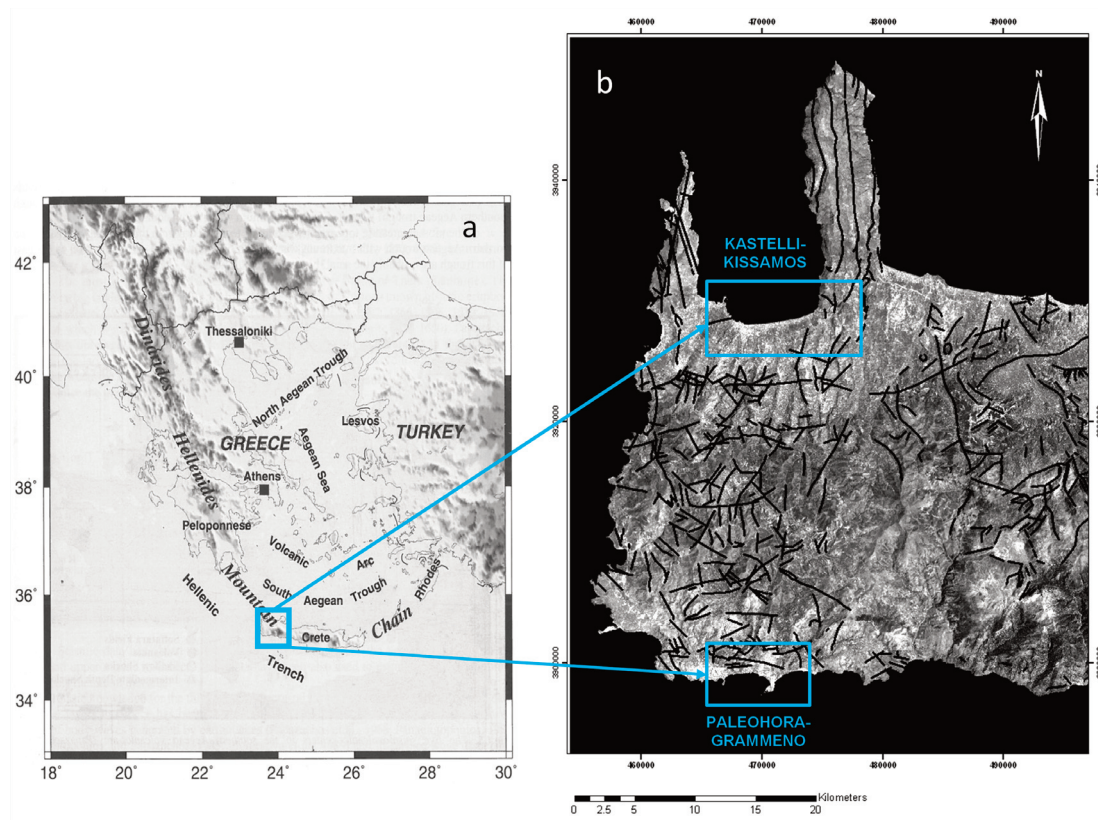
h) Cretaceous limestones in the western part of the

FIGURE 1. a) The location of Crete in the south Aegean region (Papazachos and Papazachou 1998). The blue box shows the loca–tion of the two studied areas west of Crete b) Landsat satellite image of Kastelli–Kissamou and Paleohora basins. The blue boxes indicate the investigated areas in Kissamos and Paleohora basins.

Basin (white to brown, locally compact lithographic thin bedded commonly fine grained or even microcrystalline in banks strongly karstified);

i) Cherts (red-brown seldom dark brown made up of alternating beds of radiolarites and shales with intercalations of red to blue-brown thin bedded limestone) in the southern mountainside of the Basin;

k) Limestones marbles (Metamorhic) dolomitic thin bedden limestones;

l) Cristalline Schists (Metamorhic): Shinninhg mica schists or graphitic chloritic phyllites.

The cross-section A1A2 (brown line on the map in Figure 2) is a segment of a WNW-ESE cross-section of the geological column indicating geological column variations in depth. A series of faults and fractures on a well-lithified Cretaceous limestone site in the northwest coast of the studied area occupies a sector between NNW and NNE [Moisidi, 2009; Moisidi et al., 2014] (Figure 3).

Six ERT surveys using WS and DD configurations were conducted in Kissamos (Figure 4): four ERT profiles (T1-T4) in the western and central populated area of Kastelli-Kissamou basin, two ERT profiles (T5 and T6) in the eastern zone of Kissamos (near Nopiogia/Kalidonia). Table 1 lists all of the acquisition parameters for each ERT profile, numbered as in figure 4. For the above configurations, 5 m (which is applied to acquire high-resolution data of the near surface geological structure) and 10 m electrode spacing (a deep model with high shallow resolution) was used to determine the apparent resistivities inverted to a 2D geo-electrical resistivity model.
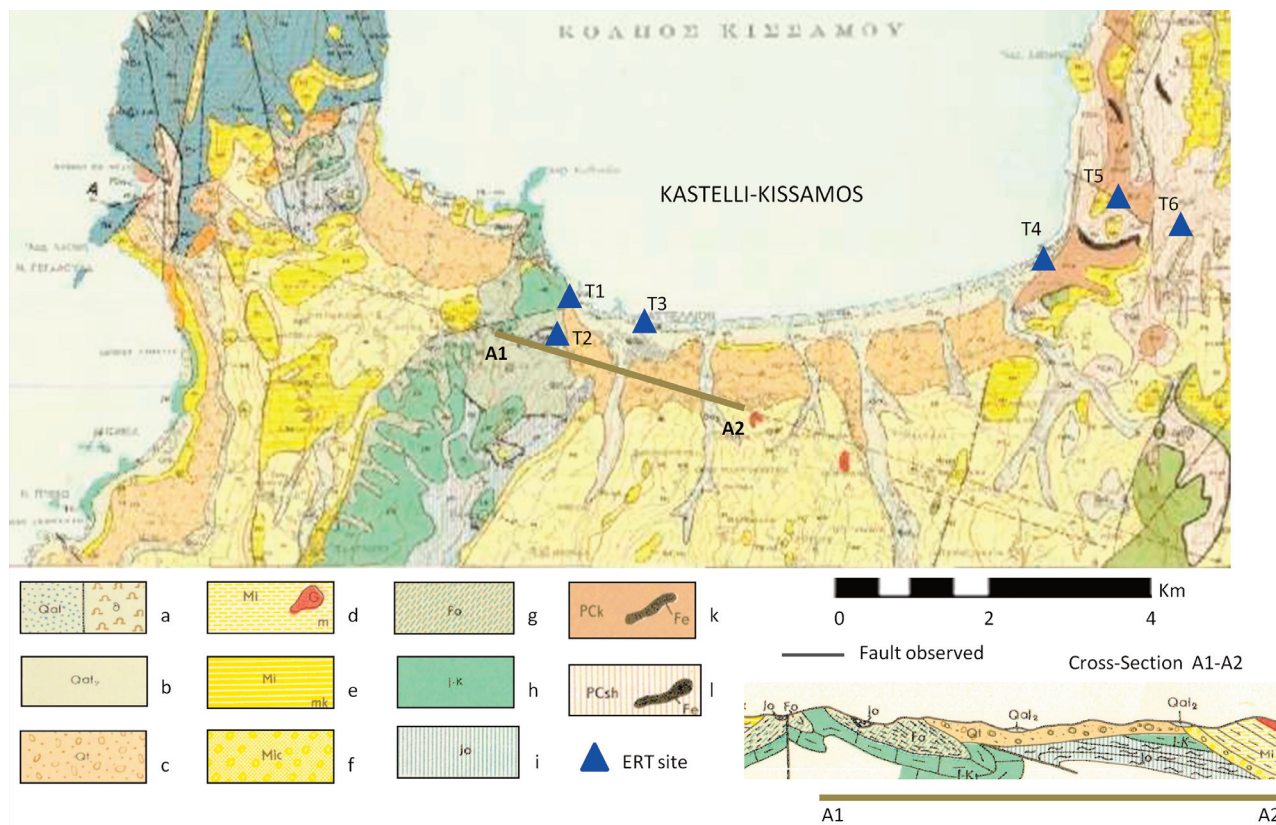
FIGURE 2. Geological map of Kastelli and Kissamos area. The geological formations of the studied area in Kastelli–Kissamos are denoted by a–l as described in the text (extracted and modified from the geological map IGSR 1970). Blue triangles indicate the approximate sites of ERT arrays. The cross section A1A2 indicates the complex geological setting characterized by lateral heterogeneities/ irregulaties and fault structure at the west part (T1–T2) of the studied area.
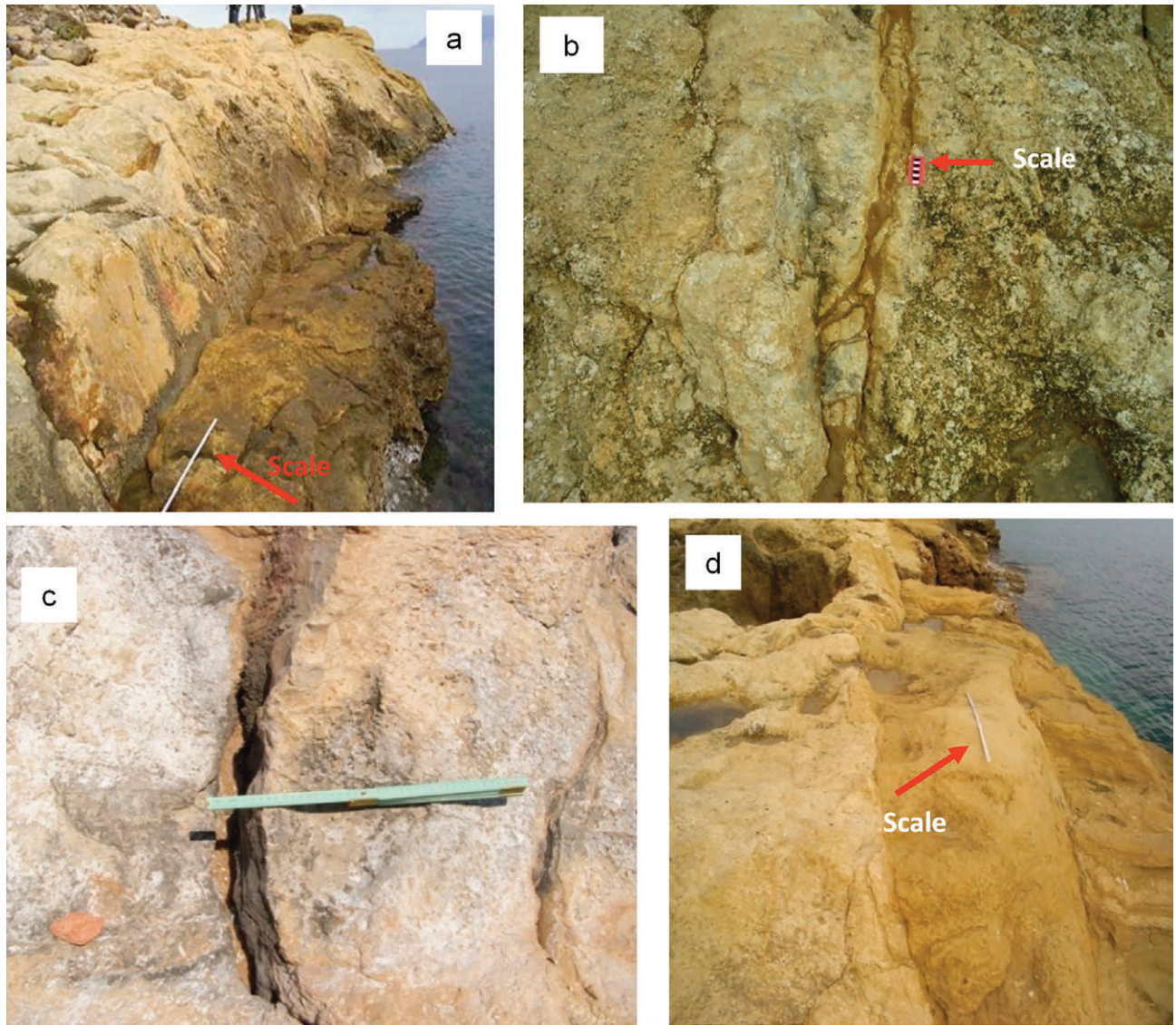
FIGURE 3. A series of faults and fractures on a well–lithified Cretaceous limestone site dominantly occupying a sector between NNW and NNE (Moisidi 2009, Moisidi et al.2014). The one meter scale is used for scale.

Profile name	Array	Length (m)	Step (m)	Datum points
T1_DD	DD	185	5	305
T1_WS	WS	185	5	227
T2_DD	DD	280	10	197
T2_WS	WS	280	10	194
T3_DD	DD	235	5	399
T3_WS	WS	235	5	312
T4_DD	DD	315	10	233
T4_WS	WS	315	10	233
T5_WS	WS	315	10	233
T6_DD	DD	315	10	233
T6_WS	WS	315	10	233

TABLE 1. List of acquisition parameters relative to the ERT profiles drawn in Figure 4.
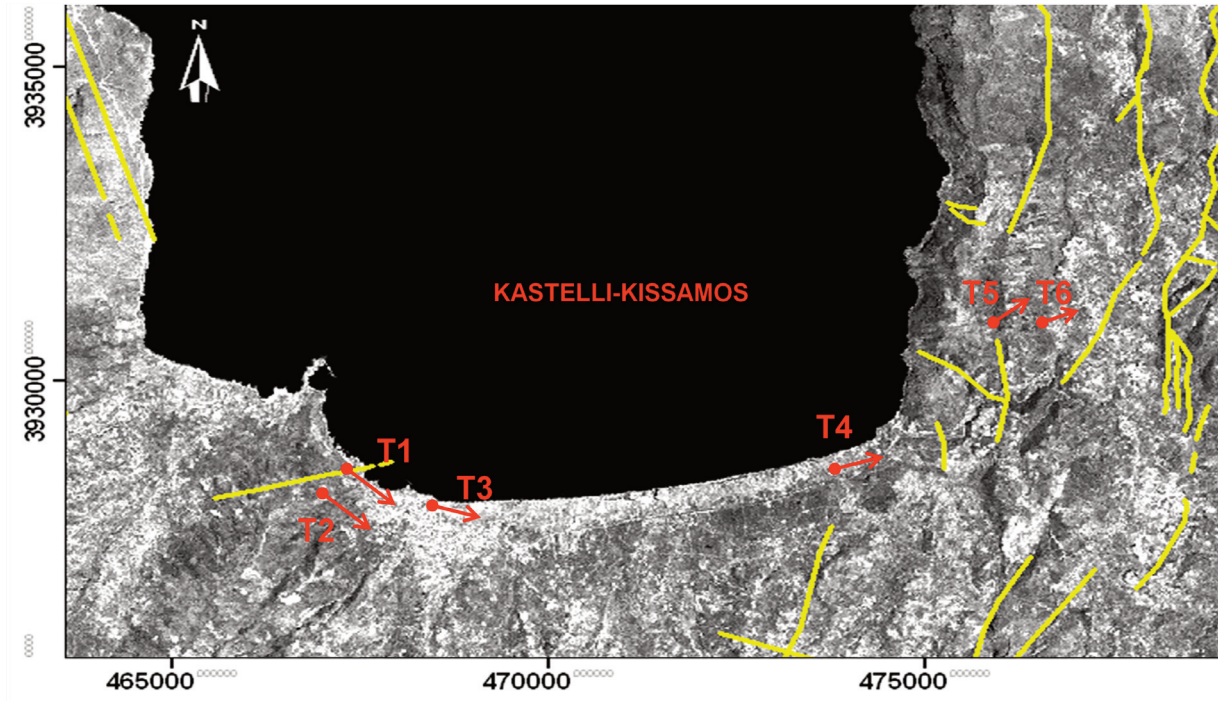
FIGURE 4. Sites where ERT profiles (T1–T6) conducted in Kissamos. The red arrows represent the orientation of the ERT profiles.

Figures 5-10 show the profiles T1-T6 in Kastelli-Kissamos basin. For each section, the measured apparent resistivity pseudosection, the calculated apparent resistivity pseudosection, the inverse model resistivity section obtained using the RES2DINV software (ERT) and the section resulting by the application of the Probability-based Electrical Resistivity Tomography (PERTI) are presented.
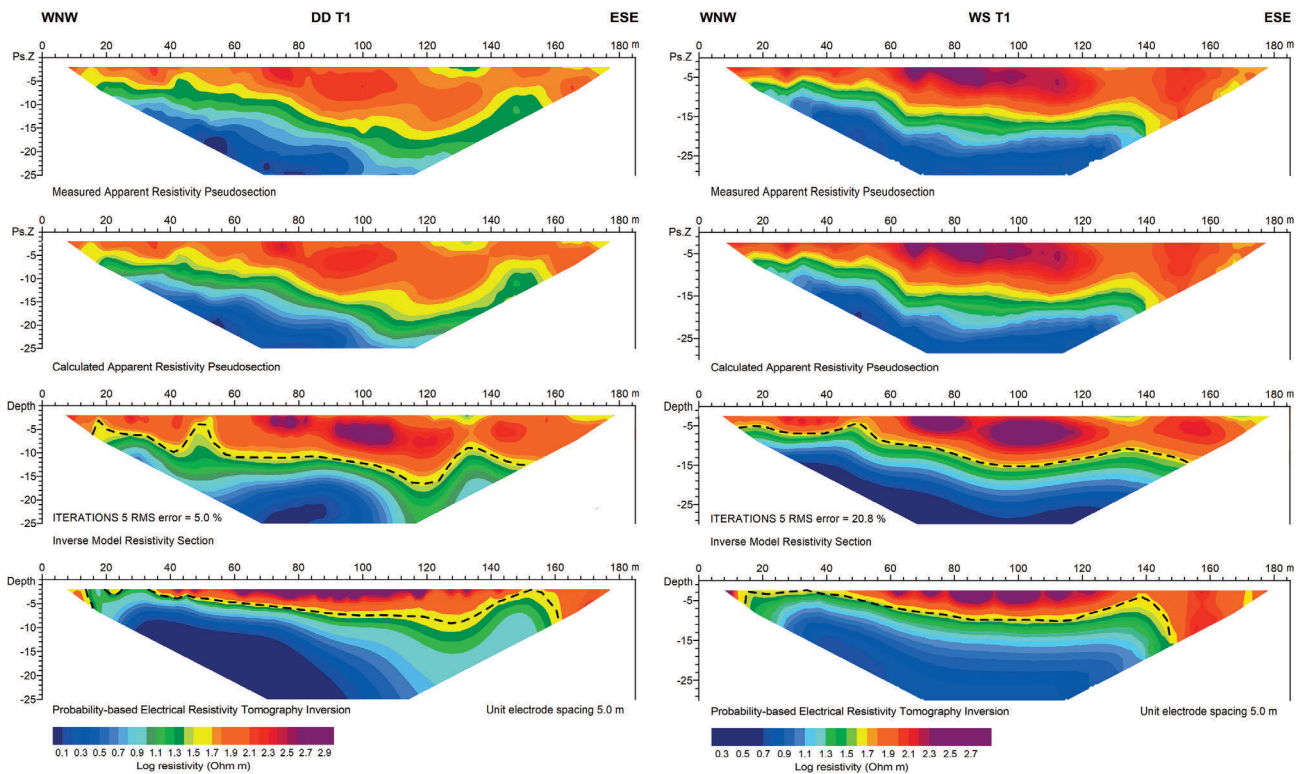

FIGURE 5. DD and WS ERT profiles at site T1.

For WS and DD profiles T1, the total length was 185 m, while an electrode spacing of 5 m was used (Figure 5). Both the ERT and PERTI profiles indicate a horizontal structure (dipping to E-SE) of a high resistive zone, with values major respect to the average resistivity, overlying a very low resistive zone (in some points less than 3.0 Ωm), below 20 m in depth, suggesting significant ground water content in sediments that is possibly saline.

The WS ERT profile images the superficial layer with a width varying between 5 m (at the origin of the line) and 17 m (at about 100 m in a horizontal distance along the profile). It tends to become less resistive below the ranges 0-20 m, 40-50 m and 130-140 m along the x-axis of the profile. The RMS of the profile using the WS array is 5.6%.

In the WS PERTI profile, the high resistive anomaly is located at 5 m in depth from 0 to 20 m along the x-axis, rises to the surface from 20 m to 40 m, deepens down to about 15 m (from 40 to 140 m where the higher resistivity are imaged), rises to the surface (at 140 m) and falls right below the 150 position on the x-axis (according to the measured apparent resistivity pseudosection). The lateral contact between the low resistivity zone (to the bottom) and the higher resistivity anomaly (to the left, or ESE, at 150 m along the x-axis) is marked by a sharp vertical

boundary that could indicate a NE-SW striking fault zone.

Both the DD ERT and DD PERTI profiles are coherent with the WS sections, with the exception of a dragging effect, typical of the DD array, that images, between 110 m and 130 m along the x-axis, a gradual deepening of the superficial resistive anomaly (until 25 m in the DD ERT and 10 m in the DD PERTI). This artefact, due probably to the dry conditions of the shallow soils, is less evident in the DD PERTI. The RMS of the ERT profile derived from the DD configuration is 21.7%. In a previous paper [Moisidi et al., 2013], at about 135 m a "speculated" N-S striking fault zone (dipping to west) is indicated by sub-vertical changes in the resistivity in the DD profile.

The DD and WS profiles T2 (Figure 6) were conducted southern of the profile T1 (see figure 4). An electrode spacing of 10 m was used and the total length was 280 m.

The DD ERT and DD PERTI profiles provide a very complex near surface structure, with a high resistive anomaly in the centre of the profile. The latter is not so visible in WS PERTI.

The DD ERT profile describes at about 140 m south of the profile (in a horizontal distance along the profile) a high vertical resistive anomaly (dipping to west) with at least 40 m width (120 m to 160 m, in a horizontal distance along the profile). The RMS error of the DD ERT line is
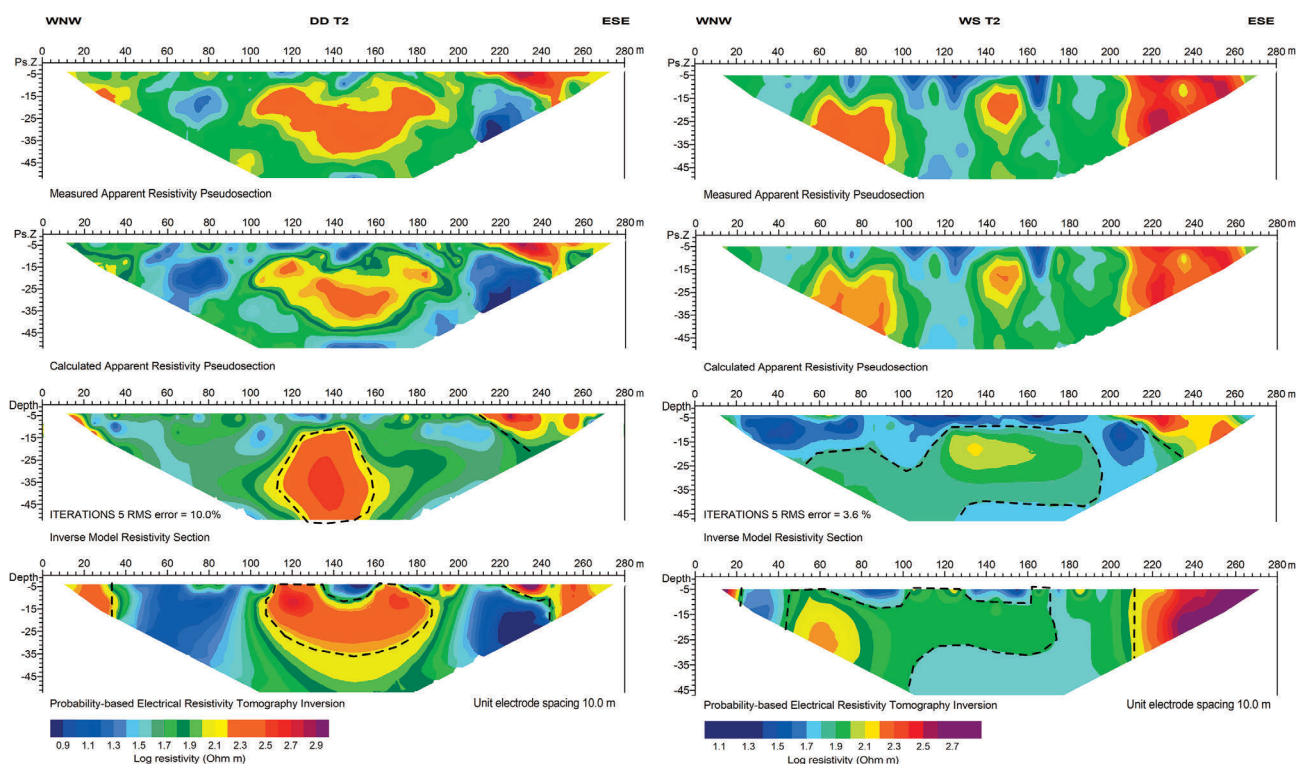

FIGURE 6. DD and WS ERT profiles at site T2.

10% after five iterations. The DD PERTI puts in evidence two shallow high resistivity nucleus located at about 120 m and 165 m along the x-axis. Taking into account the apparent resistivity pseudosection in which two inverted "V" with two legs originating from surface at the same coordinates (x=120 m and x=165 m) are visible, we can assume that two buried bodies imaged by the PERTI routine are present in that points.

Since the WS ERT and WS PERTI profiles does not presented any evidence of the previous described anomalies for both the inversion routines, we note that the above assumption is rather speculative. The WS ERT and the WS PERTI show an almost horizontal layer with medium resistivity values (1.8 Ωm to 2.2 Ωm) from about 40 m and 160 m along the x-axis ranging between 10 m and 30 m in depth. The WS PERTI also highlights a high resistive anomaly at the end of the profile (200-280 m along the line). The last one is perfectly in line with the sharp vertical boundary that could indicate a NE-SW striking fault zone revealed in T1 profile. The gap between the medium and high resistivity zone could be related to a fractured zone along the fault line in which there is an increased water content. This element, in the WS ERT profile, is shifted along the x-axis of about 20 m. In a previous paper [Moisidi et al., 2013], in corre-

spondence of the anomalous nucleus with medium resistivity values (the yellow anomaly), at about 130 m south of the profile, a N-S striking fault zone (dipping to west) is indicated by sub-vertical changes in the resistivity. We note that the WS ERT presented in Moisidi et al. [2013] shows an almost horizontal body of medium resistivities (70 Ωm to 140 Ωm) at about 120m-180m along the line with a high resistive anomaly at the end of the profile (200-280 m along the line). The RMS error of the WS ERT line is 3.6% after five iterations.

For DD and WS profiles T3 (Figure 7), an electrode spacing of 5 m was used and the total length was 235 m. In both ERT and PERTI profiles a NS striking fault zone is indicated by sub-vertical changes in the resistivity is observed at about 170 m along the profile. While the DD PERTI profile puts in evidence two shallow high resistivity bodies located at x=165 and x=190 along the line, the ERT profile images a unique almost vertical anomaly. The WS ERT and PERTI profiles show a NS striking fault zone indicate vertical changes in the resistivity at about 170 m along the profile. The surface resistivity values (till to a depth of 6 m) are ranging from 100 - 200 Ωm in both sides of the fault. In the left bottom corner of the profile, between 20 m to 160 m along profile (figure 7) and below 6 m depth, the resistivity shows very low values (<10.0 Ωm) suggesting significant
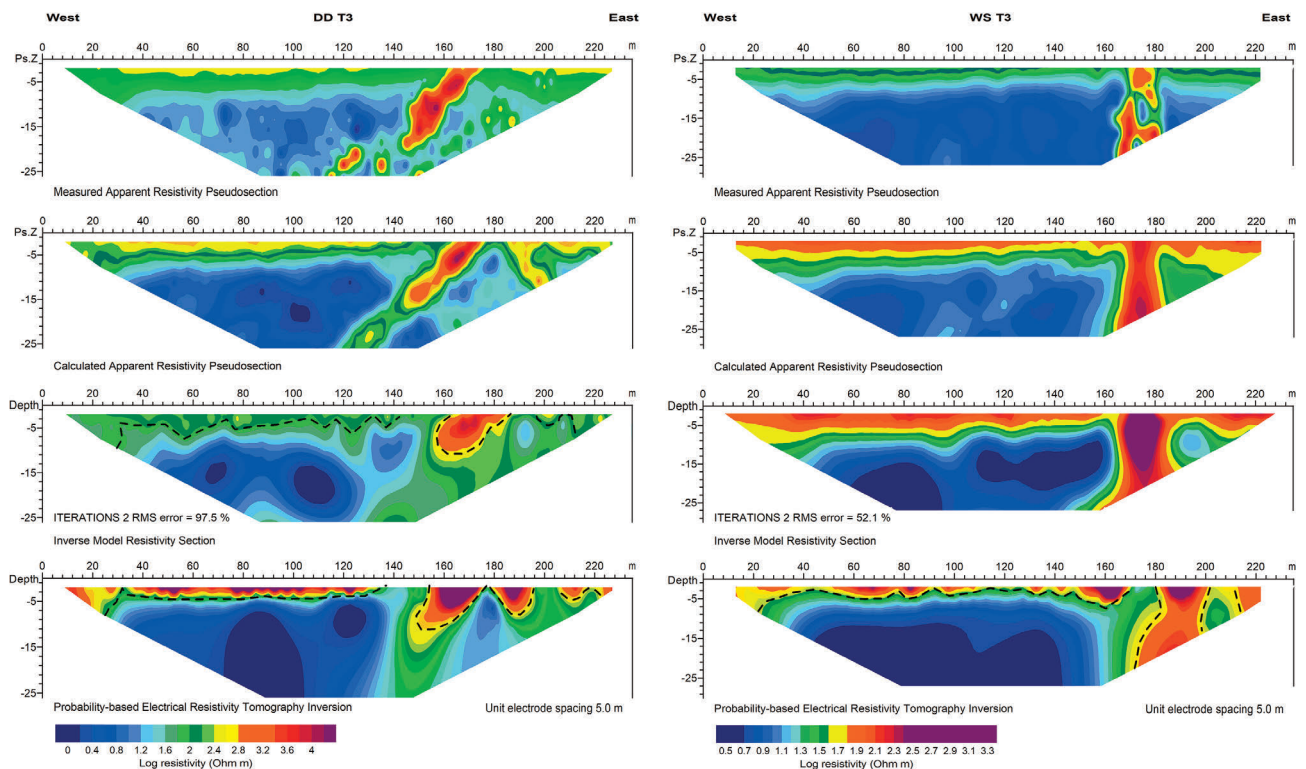

FIGURE 7. DD and WS ERT profiles at site T3.

ground water content in sediments (blue colours in Figure 9). The fault zone indicates higher resistivity values than the surroundings at about 6 m in depth and below which may suggest that it acts as a barrier to water circulations.

East of Kissamos (near Nopigia-Kalidonia), three profiles (T4, T5 and T6) were conducted (Figure 4). An electrode spacing of 10 m was used and the total length of each profile was 310 m. The results of ERT and PERTI are coherent, even if the PERTI profiles are very similar for both the electrode configuration used. For profile T4, both the routine inversions display, at about 200 m, a change from high resistivity to low resistivity that defines a NS fault zone dipping to west (figure 8). The N-S fault zone can be followed from the surface down to 40 m depth. The high resistive values correlate to Mesozoic limestones (marbles). The low resistivity zone (7-30 Ωm) could be related to an increased water content of the Quaternary deposits.

WS ERT and PERTI profiles T5 (Figure 9) put in evidence, at about 60 m to 140 m in a horizontal distance along the ERT profile, a low resistive zone striking almost NNW-SSE that can be followed from the surface down to 40 m. The high resistive values represent the surrounding host, which is characterized of Mesozoic Crystalline Schist/limestones (mar-

bles) of the Metamorphic basement of the foliated crystalline formation of Crete. The results of ERT and PERTI are coherent, even if in the ERT profile the low resistivity anomaly is shifted along the line, from left to right, of about 20 m.

ERT and PERTI profiles T6 (Figure 10) express an unconformity between the Mesozoic bedrock and the saturated Neogene sedimentary formations. The low resistivity zone (7-20 Ωm) correlates with the conductive water saturated shallow sedimentary formations. The high resistivity bedrock is present at a depth of about 25 m at 60 m along the line and gradually rises until the surface at x=220 m.

The RMS errors of the WS ERT profiles T4, T5 and T6 were 9.4% after six iterations, 5.4% after five iterations and 2.8% after five iterations, respectively.

Concluding, in the Kastelli-Kissamos area, the observed data sets present large resistivity variations that can be explained by the complex geological formations of the investigated urban areas: measurements were collected just over the calcitic bedrock (resistive body) which forms the local urban geological structure, but some part of the bedrock was fractured and fully saturated with sea-water (very conductive body).
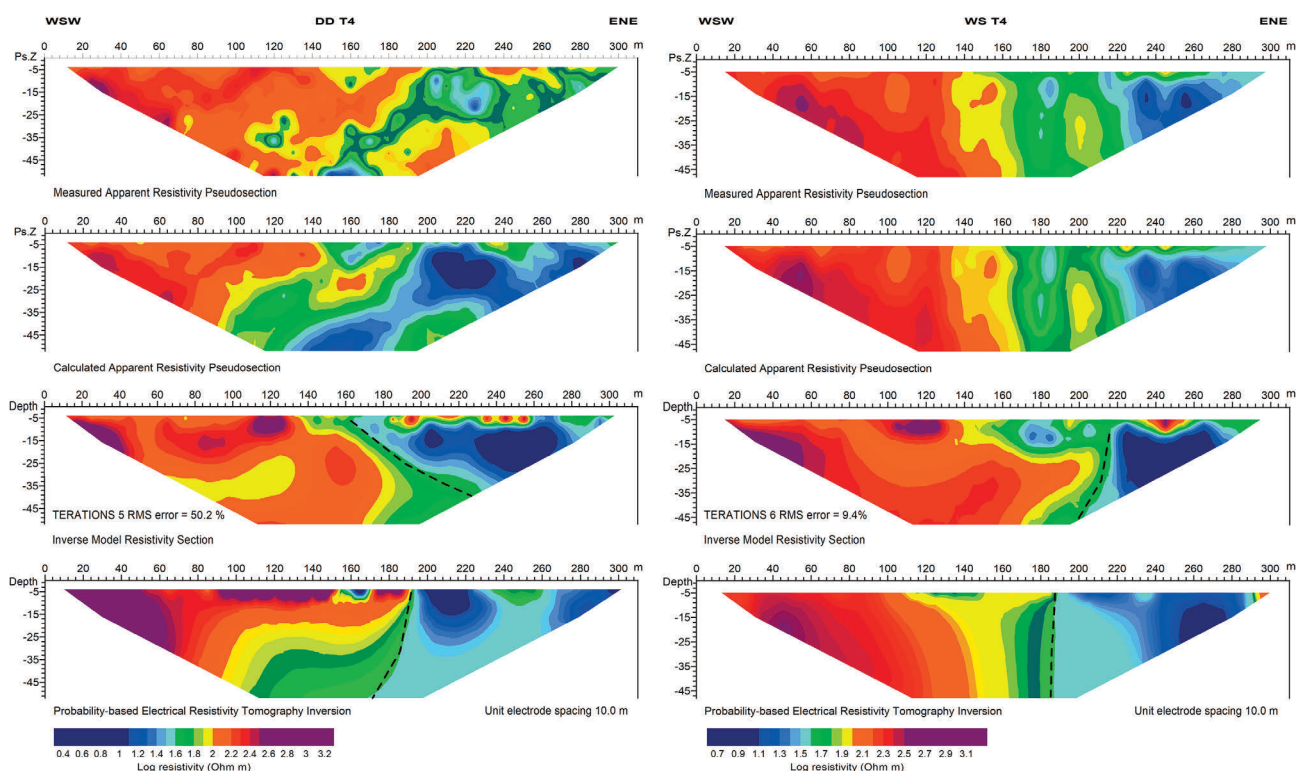

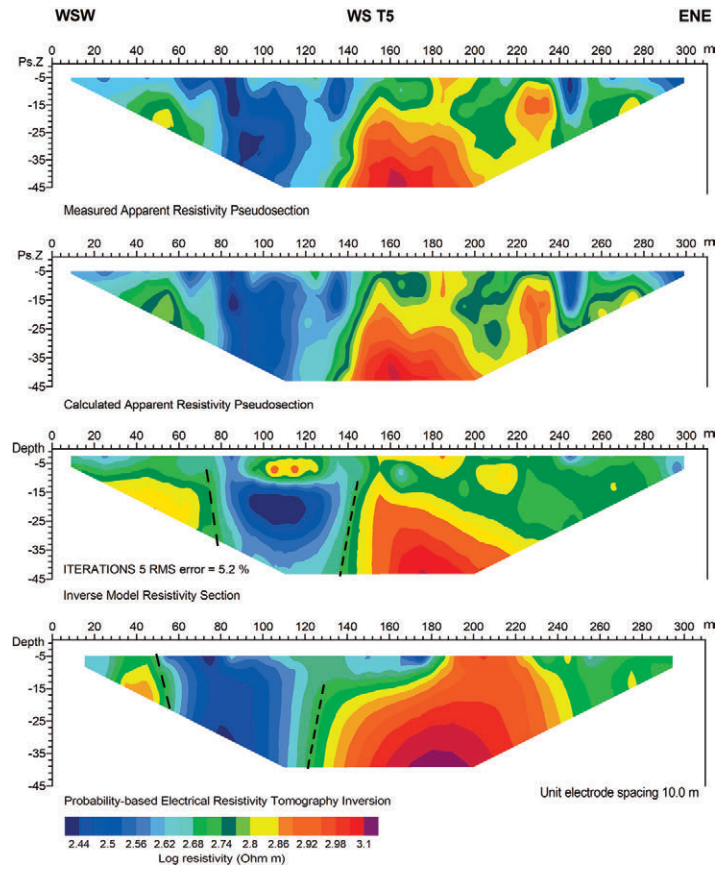FIGURE 8. DD and WS ERT profiles at site T4.
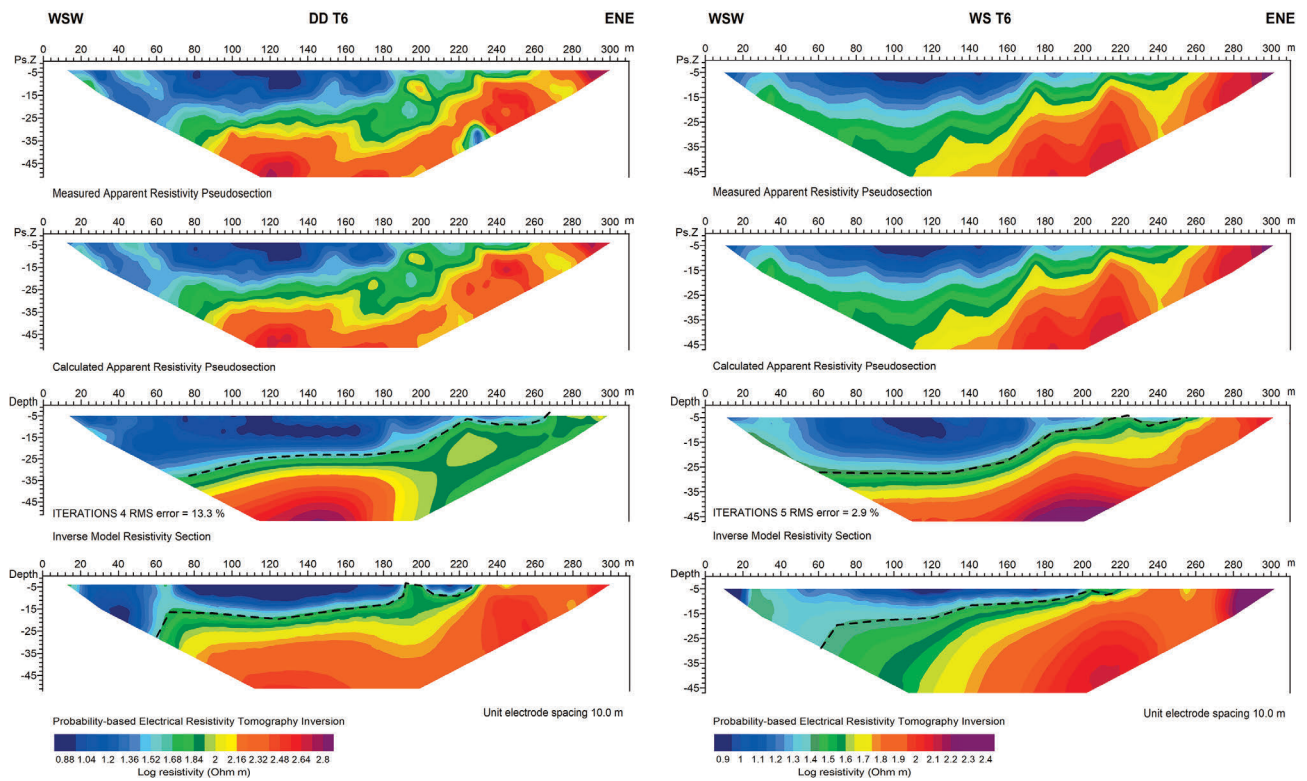
FIGURE 9. WS ERT profiles at site T5.

**FIGURE 10.** DD ERT profiles at site T6.

The fault zones revealed from ERT survey in Kastelli-Kissamou might be the extension (Figure 11, red lines) of previously imaged faults derived either from geological (Figure 4) and satellite maps (figure 11, yellow lines) provided by IGSR, [1970]. The previously imaged faults (IGSR, 1970) are located south of the basin (Figures 4 and 11, shown with yellow lines). The faults revealed from the profiles T1, T2, T3 and T4 are considered to be extensions of faults striking in a segment striking N-S to NNE-SSW denoted by F1, F2, F4 and F5, respectively (Figure 11). The fault revealed from T1 and T2 might be segments of the same fault F1 (Figure 11) and could also be related to the fault shown in the geological map with black line west of Kastelli (Figure 1). The profile T5 is

the possible extension of a fault striking N-S to NNW-SSE (denoted as F6 in Figure 11).The above fault zone delineation has been discussed in Moisidi et al. [2013].

3.2 PAHIA AMMOS-PALEOHORA AND GRAMMENO PENINSULAS

The surface geology of the investigated sites in Pahia Ammos-Paleohora and Grammeno peninsulas (IGSR 2002) (Figure 12) is characterized by:

a) Holocene alluvial deposits: clayey-sandy material and unconsolidated material of clay, sand and rubbles (Quaternary) in the centre and east of the Basin.

b) Holocene coastal sands, dunes and beach rocks
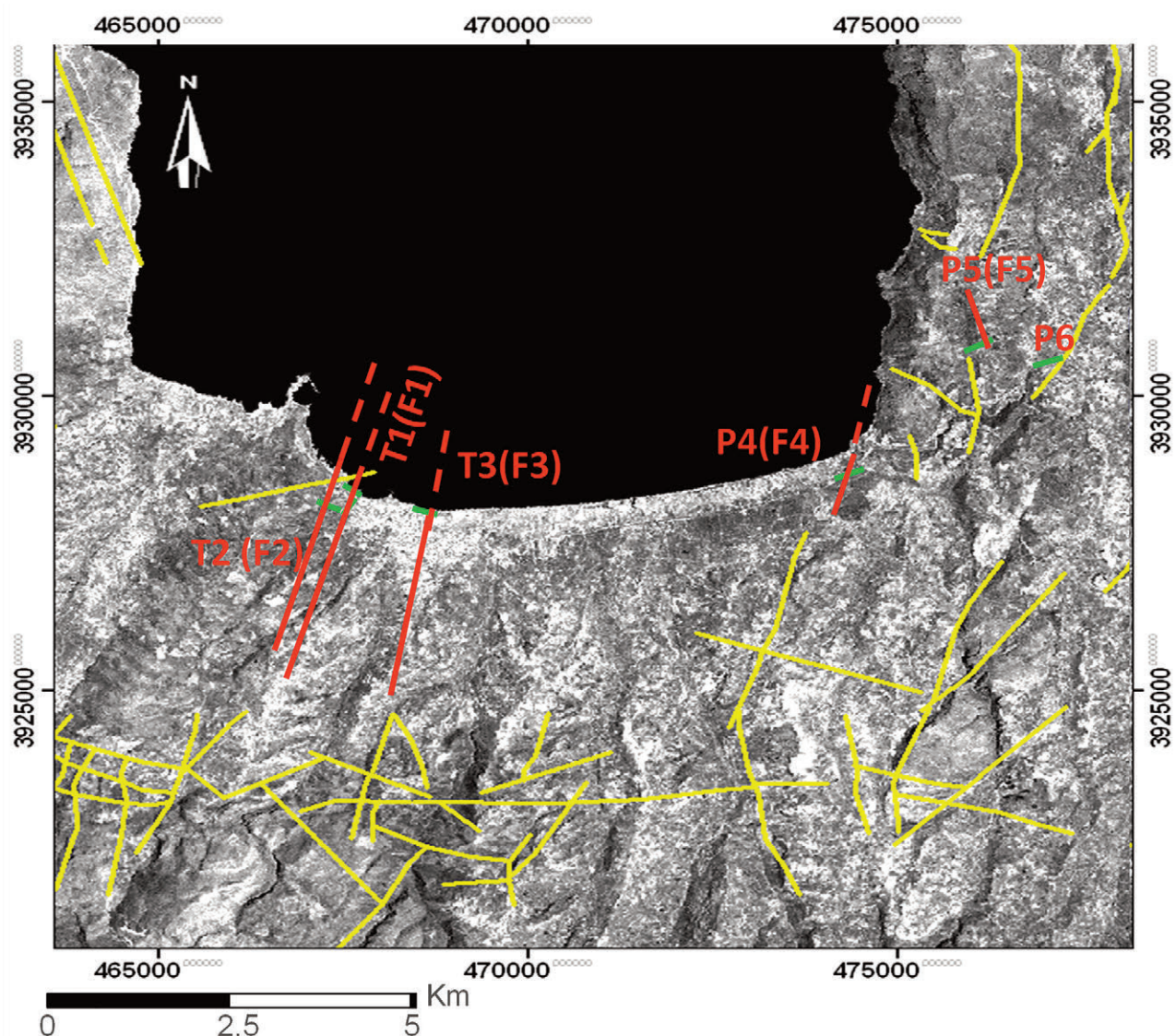
FIGURE 11. The identified faults from the cross–comparison of ERT and PERTI survey and their possible extension (red lines) of pre–viously mapped faults (yellow lines) from geological and satellite image data (IGSR (1970)). The green lines represent the orientation of the ERT profiles.

(Quaternary) in the coastline of Pahia Ammos west of Paleohora.

c) Serravalian Lissos beds: cobbles of pre-Neogene units lithified with calcitic and marly cement (Neogene, Tortonian/Pliocene) in the coastline south of Grammeno and Paleohora and northwest of Paleohora.

d) Jurrasic-Lower cretaceous Polychromatic cherts-limestones (Pindos zone: Maastrichtian) southeast and northeast of Paleohora.

e) Tripolis zone Limestones (Eocene-Oligocene), medium thick bedded and locally unbedded of grey-black colour, they are compact recrystallized with small concentration s of Fe-hydroxide, upwards they are dolomitized, locally brecciated and strongly fissured(maximum thickness 150m).

South of Paleohora two DD profiles were performed along the coast of Pahia Ammos (T7) and Grammeno peninsula (T8) to identify the near subsurface structure, which governs the coastal of two peninsulas. Table 2 lists all of the acquisition parameters for each ERT profile, numbered as in Figure 13. For the above profiles, 10 m electrode spacing was used to determine the ap-
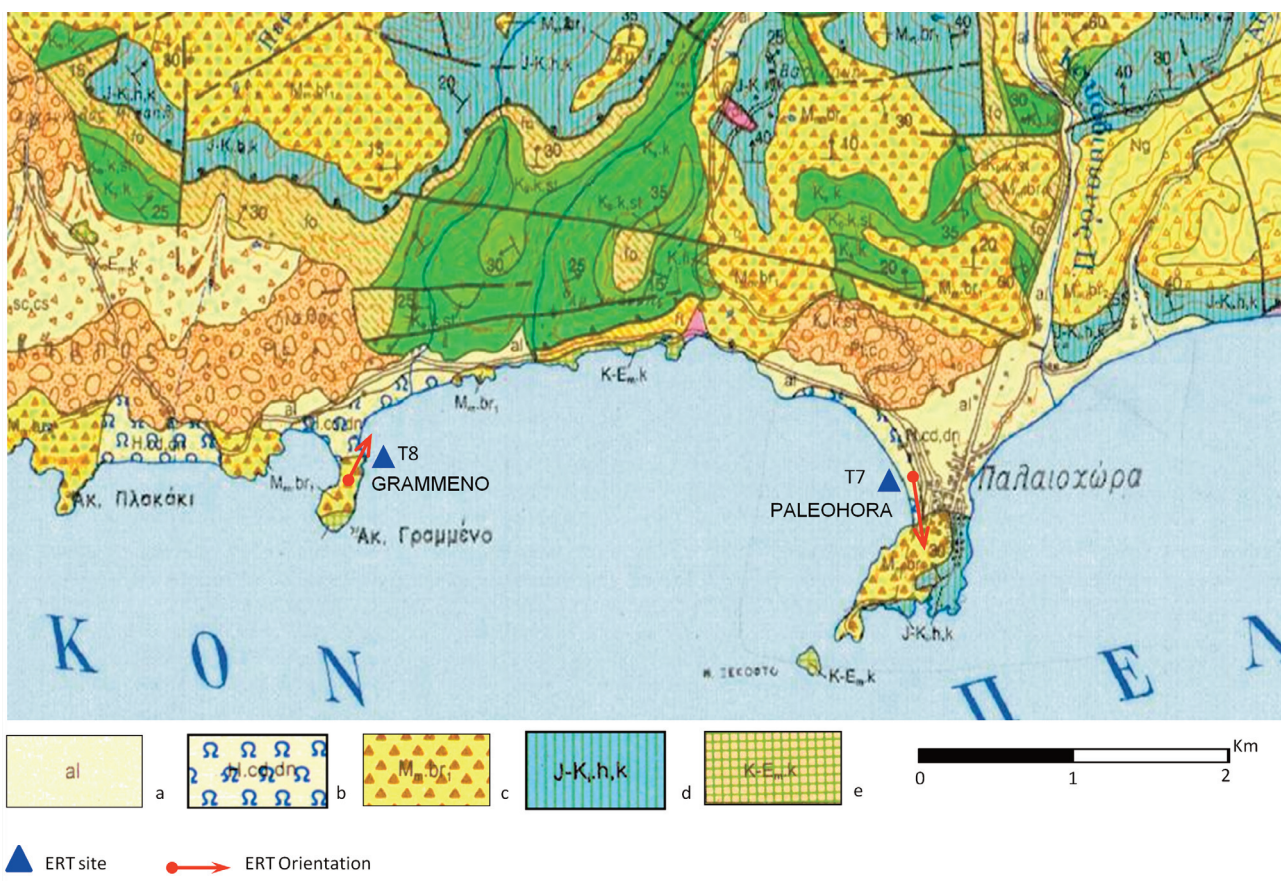

FIGURE 12. Geological map of Paleohora – Grammeno peninsulas. The geological formations of the studied area are denoted by a–e as described in the text (extracted and modified from the geological map IGSR, 2002). Blue triangles indicate the rel-ative sites of ERT arrays T7 and T8 conducted inland. Black lines represent the identified faults (extracted and modi-fied from the geological map IGSR, 2002).

Profile name	Array	Length (m)	Step (m)	Datum points
T7_DD	DD	235	10	618
T8_DD	DD	235	10	879

TABLE 2. List of acquisition parameters relative to the ERT profiles drawn in Figure 4.

parent resistivities inverted to a 2D geo-electrical resistivity model.

The DD PERTI profile T7 (figure 14, left) puts in evidence the presence of high resistivity values at the left
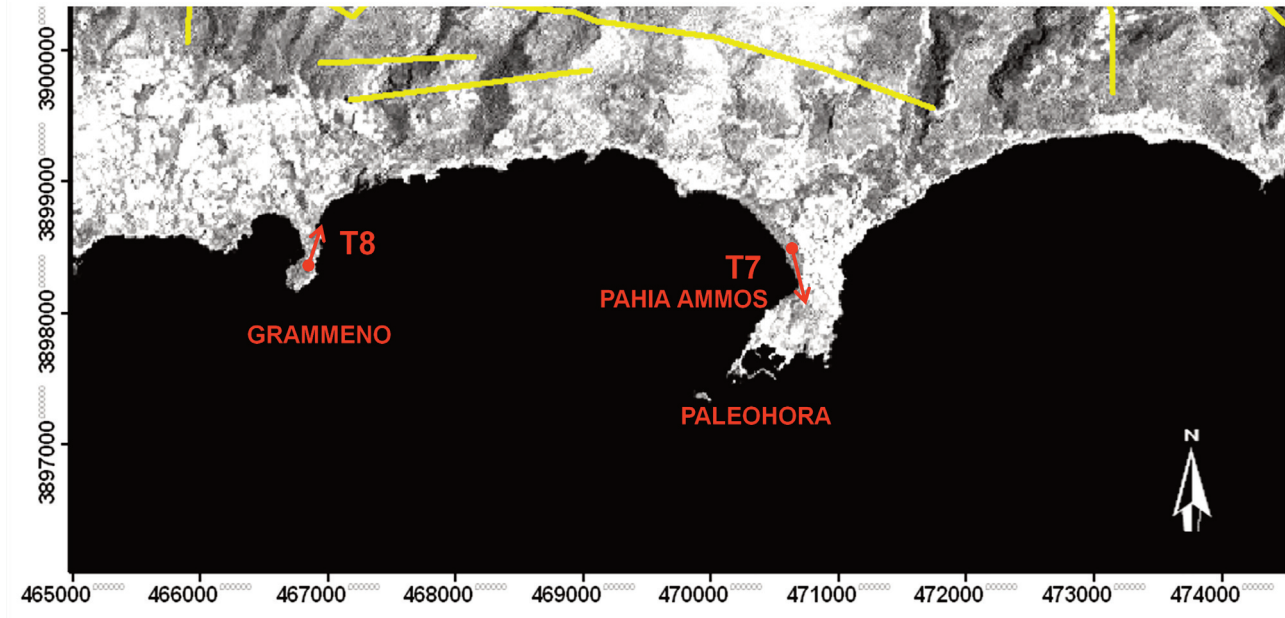

FIGURE 13. Landsat (TM8) image of the area for the ERT survey. The ERT profiles are denoted with T7 and T8. Yellow lines indi–cate the previously identified faults using geological and satellite image data (IGME 2002). The red arrows represent the orientation of the ERT profiles.
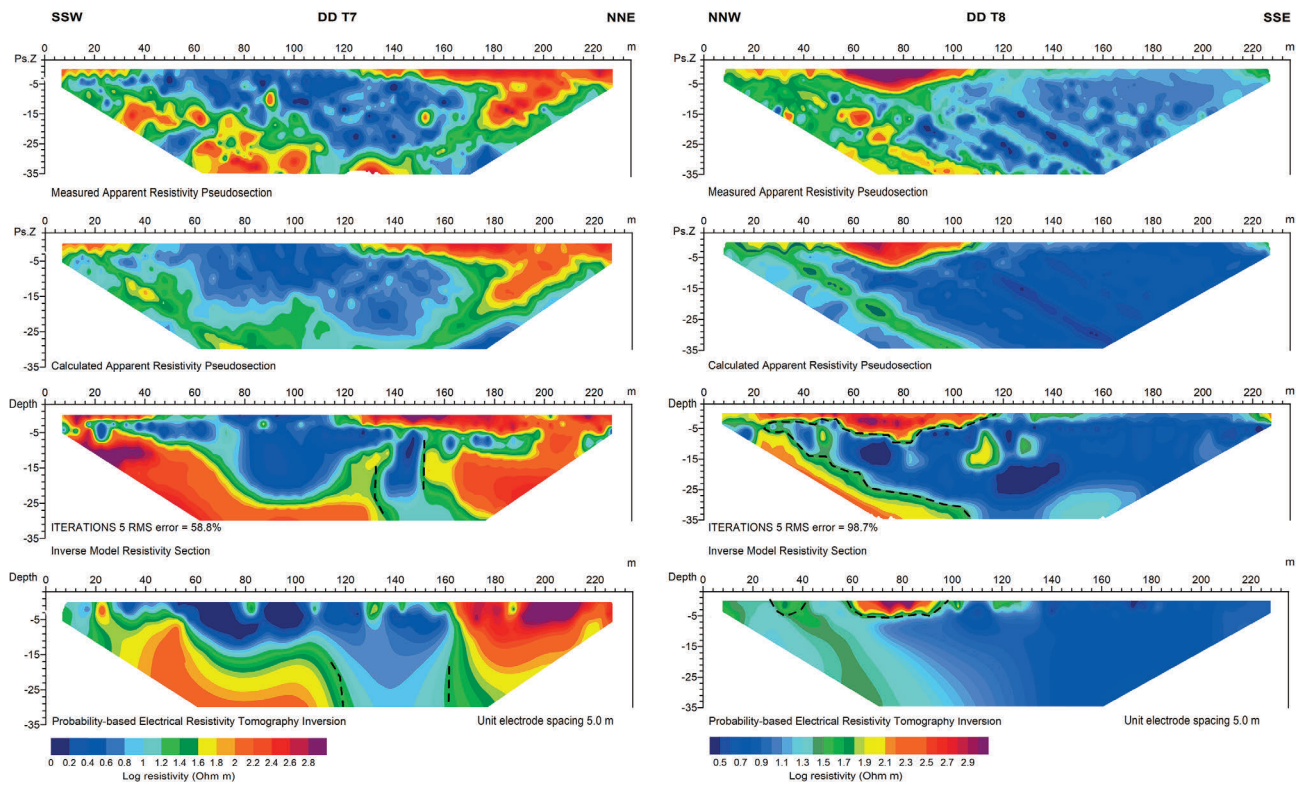

FIGURE 14. DD ERT profiles at site T7 (left) and T8 (right).

and right side of the line. The left anomaly involves the portion of soil included in the range 160-235 m along the line and it has a significant lateral variation and a vertical boundary. The high electrical resistivity values correlate with the electrical physical properties of the limestone/calcitic bedrock. Elsewhere conductive materials are present and, considering the resistivity values and the location of the profile (along and close to the coastline), it can be assumed that the fractured zone is saturated with saltwater. Similarly the DD ERT profile images (Figure 14, left) presents an oblique anomaly in the left side that is probably due to a dragging effect of the DD array used during acquisition and it reflects the left leg of the inverted "V" visible in the apparent resistivity pseudosection originating from the surface at x=210 m along the line.

The DD ERT and PERTI profiles T8 enhance to highlight a shallow high resistivity concentrated above all in the range 60-100 m along the line (Figure 14, right). While the PERTI images a section in which the conductive resistivity values prevail in all the section, the ERT puts in evidence in the left side an oblique high resistivity anomaly originating from the surface at x=20 m along the line. This diverse could be viewed along with the comment presented in Mauriello and Patella [2009] on the limits of RES2DINV to present the very shallow structures, while PERTI results present such an ability.

In conclusion, in the Grammeno and Paleohora area, the very complex 3-D near subsurface heterogeneities and irregularities caused serious distortion in the lower part of the resulted tomographic model. Those aspects caused the insertion of high RMS (58.8 % in T7 and 98.7 % in T8) in the calculated models by the RES2DINV software during its effort to fit the high variability of measured resistivity. The T7 profile puts in evidence a probable fractured zone saturated with salt water, while the T8 profile (considering the cross-comparison of ERT and PERTI) does not give any information about the presence of faults. Elsewhere conductive materials are present and, considering the resistivity values and the location of the profile (along and close to the coastline), it can be assumed that the fracture zone is saturated with saltwater.

4. CONCLUSION

As outlined in previous applications [Amato et. al., 2016; Compare et al., 2009a, 2009b; Cozzolino et al., 2012, 2014; Rose et al., 2015], the PERTI method can be considered a self-sufficient procedure, useful to delineate location and shape of the most probable sources of the anomalies detected on the ground surface. The independence from *a priori* information, the absence of iterative processes, the drastic reduction of computing time with respect to standard deterministic inversion tools, the independence from data acquisition techniques and spatial regularity, the capability to resolve complex continuous resistivity variation make the PERTI algorithm a versatile and objective approach.

While the RAOP algorithm [Mauriello and Patella, 1999] was used to imagine faults and geological formations [Alaia et al., 2009; Valente et al., 2018], the PERTI routine is here used for the first time. As testified by the comparison between ERT obtained with the RES2DINV commercial software, the PERTI procedure provided a good performance in drawing geological sections. In different cases, it has been proved that the probability algorithm is independent of the technique used for their acquisition (WS or DD arrays) and acts as an intrinsic filter. It is the circumstance well evident in T1, T2, T7 and T8 profiles in the measured data sets presented in this work. While the ERT obtained with the RES2DINV is in same cases strongly influenced by noise and correlated phantom effects, the PERTI result provides a simultaneous smoothing of the uncorrelated noise and the highlighting of the most representative image of the geological stratigraphy. In principle, this property derives from the circumstance that such types of disturbances have zero probability of being associated with true anomaly sources within the context of the geoelectrical theory.

In general, the results of the applications in Kastelli-Kissamos basin (northwest Crete) and Paleohora basin (southwest Crete) enabled the delineation of shallow fractures in the complex geological environment of the investigated urban areas.

The Kastelli-Kissamos area is characterized by the presence of complex geological formations, testified by the large resistivity variations in the measured data sets, in which there is evidence of a calcitic bedrock that, in some points, is fractured and fully saturated with seawater. Profiles T1, T2, T3, T4 and T5 enhances the occurrence of sub-vertical contacts between the high resistivity bedrock (calcilitic bedrock) and lower resistivity zones. The comparison between the resistivity topographies, the geological and the satellite map (provided by IGSR) allows to state that the boundaries of the anomalies can be related to fault zones.

In particular T1, T2, T3 and T4 results can be extensions of faults zones striking in a segment N-S to NNE-SSW (respectively denoted by F1, F2, F4 and F5 in Figure 11) and T5 results to the N-S to NNW- SSE striking fault (denoted as F6 in Figure 11). Figure 11 indi-

cates south of the studied area the presence of fault zones (yellow lines) striking in a segment N-S to NE-SW. Therefore, it is highly prone that the defined fault zones north of the studied area are those faults possible extended from south.

T6 profile does not give any information about the presence of fractures as attested by the cross-comparison of ERT and PERTI results.

The Grammeno and Paleohora area presents very a complex 3-D near subsurface stratigraphy testified by the numerous distortions in the lower part of the resulted tomographic models. While the T8 profile does not put in evidence relevant anomalies, the T7 profile reveals a probable fractured zone saturated with salt water.

Considering that active and inactive faults can behave as a wave-guides in an impinging seismic wave front [Cornier and Spudich, 1984] the delineation of faults particular in urban areas is of importance in seismic hazards studies. The overall scenario reconstructed with this study allowed to identify the presence of relevant coseismic effects (shallow faults) and to define, at a sufficiently detailed scale, the stratigraphic and structural features in the two investigated urban perimeters, with particular regard to the reconstruction of thicknesses and geometries of the substrate units, beach or alluvial deposits. The results therefore represent a basic tool that should be carefully acknowledged in assessing local seismic hazard as a function of urban reconstruction and planning projects.

REFERENCES

Alaia R., D. Patella and P. Mauriello (2008). Application of the geoelectrical 3D probability tomography in a test-site of the archaeological park of Pompei (Naples, Italy), J. Geophys. Engin., 5, 67-76.

Amato V., M. Cozzolino, G. De Benedittis, G. Di Paola, V. Gentile, C. Giordano, P. Marino, C.M. Rosskopf and E. Valente (2016). An integrated quantitative approach to assess the archaeological heritage in highly anthropized areas: the case study of Aesernia (southern Italy), ACTA IMECO, 5 (2), 33-43.

Armijo R., H. Lyon-Caen and D. Papanastassiou D. (1992). East-west extension and Holocene normal fault scarps in the Hellenic arc, Geol, 20, 491-494.

Caputo R., S. Pitsitelli, A. Oliveto, E. Rizzo and V. Lapenna (2003). The use of electrical resistivity tomographies in active tectonics: examples from the Tyrnavos Basin, Greece, J. Geodyn, 36, 19-35.

Caputo R., L. Salviulo, S. Pitsitelli and A. Loperte

(2007). Late Quaternary activity along the Scorciabuoi Fault (southern Italy) as inferred from electrical resistivity tomographies, Ann. Geophys, 50, 213-224.

Constable S., R. Parker and C. Constable (1987). Occam's inversion: A practical algorithm for generating smooth models from electromagnetic sounding data, Geophys, 5, 289-300.

deGroot-Hedlin C. and S. Constable (1990). Occam's inversion to generate smooth, 2D models from magnetotelluric data, Geophys, 55, 1613-1624.

Compare V., M. Cozzolino, P. Mauriello and D. Patella (2009a). 3D Resistivity probability tomography at the prehistoric site of Grotta Reali (Molise, Italy), Archaeol. Prospect., 16 (1), 53-63.

Compare V., M. Cozzolino, P. Mauriello and D. Patella (2009b). Resistivity probability tomography at the Castle of Zena (Italy), J. Im. Video Process., Eurasip, 693274, 1-9, doi: 10.1155/2009/693274.

Cornier V. and P. Spudich (1984). Amplification of ground motion and waveform complexity in fault zones: examples from the San Andreas and Calaveras fault zones, Geophys. J. R. Astron. Soc., 79, 135-152.

Cozzolino M., E. Di Giovanni, P. Mauriello, A. Vanni Desideri and D. Patella (2012). Resistivity tomography in the Park of Pratolino at Vaglia (Florence, Italy), Archaeol. Prospect., 19 (4), 253-260.

Cozzolino M., P. Mauriello and D. Patella (2014). Resistivity Tomography Imaging of the substratum of the Bedestan Monumental Complex at Nicosia, Cyprus, Archaeom., 56 (2), 331-350.

Dahlin T. (2001). The development of electrical imaging techniques, Compu. Geosci., 27, 1019-1029.

Demanet D., F. Renardy, K. Vanneste, D. Jongmas, T. Camelbeek and M. Meghraoui(2001). The use of geophysical prospecting for imaging active faults in the Roer Graben, Belgium, Geophys, 614, 78-89.

Duermeijer C. E., M. Nyst, P. T. Meijer, C. G. Langereis and W. Spakman (2000). Neogene evolution of the Aegean arc: paleomagnetic and geodetic evidence for a rapid and young rotation phase, Earth Planet. Sci. Lett., 176, 509-525.

Fazzito S. Y., A. E. Rapalini, J. M. Cortés and C. M. Terrizzano (2009). Characterization of Quaternary Faults by Electric Resistivity Tomography in the Andean Precordillera of Western Argentina, J. South Am. Earth Sci, 28 (3), 217-228.

Fassoulas C. (2001). The tectonic development of a Neogene basin at the leading edge of the active

European margin:the Heraklion basin, Crete, Greece, J.Geod., 31, 49-70.

Georgaki I., P. Soupios, N. Sakkas, F. Ververidis, E. Trantas, F. Vallianatos and T. Manios T. (2008). Evaluating the use of electrical resistivity imaging technique for improving CH4 and CO2 emission rate estimations in landfills, Sci. Total Environ., 389, 522-531.

Hatzfeld D., M. Besnard, K. Makropoulos, N. Voulgaris, V. Kouskouna, P. Hatzidimitriou, P. Panagiotopoulos, G. Karakaisis, A. Deschamps and H. Lyon-Caen (1993). Subcrustal microearthquake seismicity and fault plane solutions beneath the Hellenic arc, J. Geophys. Res., 98, 9861-9870.

Institute for Geology and Subsurface Research (IGSR) (1970). Geological map of Greece, Kastelli Sheet (Geological survey conducted by Karageorgiou E, 1:50.000 scale).

Institute of Geology and Mineral Exploration (IGME) (2002). Geological map of Greece, Paleohora Sheet (Geological survey conducted by Tsalahouri E and Fontou C 1:50.000 scale).

Jackson J. (1994). Active tectonics of the Aegean region, Annu. Revis. Earth Planet Sci., 22, 239-271.

Jost M., O. Knabenbauer, J. Cheng and H.P. Harjes (2002). Fault plane solutions of microearthquakes and small events in the Hellenic Arc, Tectonophys, 356, 87-114.

Lapenna V., P. Pietro, A. Perrone, S. Piscitelli, F. Sdao and E. Rizzo (2003). High resolution geoelectrical tomographies in the study of Giarrossa landslide (southern Italy), Bull. Eng. Geol., 62, 259-268.

LePichon X., N. Chamot-Rooke and N. Lallemant (1995). Geodetic determination of the kinematics of central Greece with respect to Europe, J Geophys Res., 100, 675-690.

Loke M. H. and R. D. Barker (1995). Least-squares deconvolution of apparent resistivity pseudosection, Geophys., 60, 1682-1690.

Loke M. H. and R. D. Barker (1996a). Rapid least-squares inversion of apparent resistivity pseudosections by a quasi-Newton method, Geophys. Prospect., 44, 131-152.

Loke M. H. and R. D. Barker (1996b). Practical techniques for 3D resistivity surveys and data inversion, Geophys. Prospect., 44, 499-523.

Loke M.H. (2004). Tutorial: 2-D and 3-D electrical imaging surveys. Geotomo Softwares, Penang, Malaysia. www.geotomosoft.com

Martinez J.J., J. L. Benavente García-Arostegui, M.C.

Hidalgo and J. Rey (2009). Contribution of electrical resistivity tomography to the study of detrital aquifers affected by seawater intrusion-extrusion effects: The river Velez delta (southern Spain), Eng. Geol., 108, 161-168.

Marescot L., S. P. Lopes, S. Rigobert and A. G. Green (2008). Nonlinear inversion of geoelectric data acquired across 3D objects using a finite-element approach, Geophys., 73 (3), 121-133.

Margiotta S. and S. Negri (2008). Stratigraphic and geophysical integrated methodologies for the interpretation of sulphur water formational environment in Salento (Italy), Int. J. Coal Geol., 75, 27-39.

Mauriello P. and D. Patella (1999). Resistivity anomaly imaging by probability tomography, in Geophysic. Prospec., 47(3), 411-429.

Mauriello P. and D. Patella D. (2009). A data-adaptive probability-based fast ERT inversion method, Prog. Electromagn. Res. 97, 275-90.

McKenzie D.P. (1978). Active tectonics of the Alpine-Himalayan belt: the Aegean Sea and surrounding regions, Geophys. J. R. Astron. Soc., 55, 217-254.

Meads N. L., L. R. Bentley and C. A. Mendoza. (2003). Application of electrical resistivity imaging to the development of a geologic model for a proposed Edmonton landfill site, Can. Geotechn. J., 40, 551-558.

Meier T., D. Becker, M. Endrun, M. Rische, M. Bohnhoff, B. Stöckhert and H. P. Harjes (2007). A model for the Hellenic subduction zone in the area of Crete based on seismological investigations, Geol. Soc. Lond. Special Publications, 291, 183-199.

Mouslopoulou V., C. Andreou, K. Atakan and I. Fountoulis (2001). Paleoseismological investigations along the Kera fault zone, Western Crete: Implications for seismic Hazards Assesment, Bull. Geol. Soc. Greece, Proc of the 9th Int Congr 4 XXIV, 1531-1537.

Moisidi M., F. Vallianatos Soupios P. and Kershaw S. (2012). Spatial spectral variations of microtremors and electrical resistivity tomography surveys for fault determination in southwestern Crete, Greece, J Geophys Eng, 9 (3), 261-270.

Moisidi M., F. Vallianatos, P. Soupios, S. Kershaw, D. Rust and S. Piscitelli (2013). Modelling tectonic features of the Kissamos and Paleohora areas, Western Crete (Greece): combining geological and geophysical surveys, J. Geophys. Eng., 10 (2), 025015.

Nguyen F., S. Garambois, D. Jongmans, E. Pirard and M. H. Loke (2005). Image processing of 2D resistivity data for imaging faults, J. Appl. Geophys., 57, 260-277.

Nguyen F., S. Garambois, D. Chardon, D. Hermitte, O. Bellier and D. Jongmans (2007). Subsurface electrical imaging of anisotropic formations affected by a slow active reverse fault, Provence, France, J. Appl. Geophys., 62, 338-353.

Papadopoulos N. G., Tsourlos P., Tsokas G. N. and Sarris A. (2006). Two-dimensional and threedimensional resistivity imaging in archaeological site investigation, Archaeol. Prospect., 13, 163-181.

Papazachos B. C. and A. A. Kiratzi (1996). A detailed study of the active crustal deformation in the Aegean and surrounding area, Tectonophys, 253, 129-153.

Papazachos B. C. and C.C. Papazachou (1997). Earthquakes of Greece, Thessaloniki: Ziti Editions, 304.

Patella D. (1997). Introduction to ground surface self-potential tomography, Geophys. Prospect. 45,653-681.

Pidlisecky A., E. Haber and R. Knight (2007). RESINVM3D: a 3D resistivity inversion package, Geophys., 72, 2, H1-H10.

Rahl J. M., C. Fassoulas and T. Brandon (2004). Exhumation of high pressure metamorphic rock within an active convergent margin, Crete, Greece, in 32th Int. Geol. Congr., Field guide B32, 2, 3-36.

Rizzo E., A. Colella, V. Lapenna and S. Piscitelli (2004). High-resolution images of the fault-controlled High Agri Valley basin (Southern Italy) with deep and shallow electrical resistivity tomographies, Phys. Chem. Earth., 29, 321-327.

Rose D., M. Cozzolino and P. Mauriello (2015). Preliminary notes of the research on the Roman aqueduct of Alba Fucens (AQ) in Italy. The geophysical prospecting in the study of the free-flowing channel and the inverted siphon, in Babesch (Bulletin Antieke Beschaving), Annual Papers on Mediterranean Archaeology, 27, 107-112.

Sasaki Y. (1989). 2-D joint inversion of magnetotelluric and dipole-dipole resistivity data, Geophys 54, 254-262.

Sasaki Y. (1992). Resolution of resistivity tomography inferred from numerical simulation, Geophys. Prospect., 40, 453-46.

Sasaki Y. (2006). 3-D resistivity inversion using a subspace method, Geophys. Explor., 59(5), 425-430.

Seidel M., E. Seidel, B. St ckhert (2007). Tectono-sedimentary evolution of Lower to Middle Miocene half-graben basins related to an extensional detachment fault (western Crete, Greece), Terra Nova, 19, 39-47.

Soupios P., S. Piscitelli, F. Vallianatos and V. Lapenna (2008). Contamination delineation and characterization of waste disposal sites performing integrated and innovative geophysical methods, Waste management research trends (ed Toma V.Golush), 2nd Quarter, Nova Publish USA.

Storz H. W., W. Storz and F. Jacobs (2000). Electrical resistivity tomography to investigate geological structures of the earth's upper crust, Geophys. Prospect., 48, 455-471.

ten Veen J. H. and G. Postma (1999a). Roll-back controlled vertical movements of outer-arc basins of the Hellenic subduction zone (Crete, Greece), Basin Res., 11, 243-266.

ten Veen J. H. and G. Postma (1999b). Neogene tectonics and basin fill patterns in the Hellenic outerarc, Basin Res., 11, 223-241.

ten Veen J. H. and K. Kleinspehn (2003). Incipient continental collision and plate-boundary curvature: Late Pliocene-Holocene transtensional Hellenic forearc, Crete, Greece, J. Geol. Soc. Lond., 160, 161-181.

Tsourlos P. (1995). Modeling interpretation and inversion of multi-electrode resistivity survey data, Phd Thesis, University of York.

Tsourlos P. and R. Ogilvy (1999). An algorithm for the 3-D Inversion of Tomographic Resistivity and Induced Polarization data: Preliminary Results, J. Balkan Geophys. Soc., 2, 30-45.

Valente E., A. Ascione, G. Ciotoli, M. Cozzolino, S. Porfido S. and A. Sciarra (2017). Do moderate magnitude earthquakes generate seismically induced ground effects? The case study of the M_w = 5.16, 29th December 2013 Matese earthquake (southern Apennines, Italy), I. J. Earth Sci., 1-21.

van Hinsbergen D. J. and J. E. Meulenkamp (2006). Neogene supra-detachment basin development on Crete (Greece) during exhumation of the South Aegean core complex, Basin Res, 18, 103-124.

van Schoor M. (2002). Detection of sinkholes using 2D electrical resistivity imaging, J. Appl. Geophys., 50, 393-399.

Wise D. J. and C. S. Cassidy (2003). Geophysical imaging of the Quaternary Wairoa North Fault, New Zealand: a case study, J. Appl. Geophys., 53, 1-16.

*CORRESPONDING AUTHOR: Marilena COZZOLINO;
Institute of Technologies Applied to Cultural Heritage, CNR,
Monterotondo, Roma, Italia,
email: marilena.cozzolino@itabc.cnr.it